

Power Generation from Localized Wind Energy in Expressways

Saeed Nazari¹, Dr. Irene Vrbik^{2*}

¹M.A.Sc. Student in Mechanical Engineering at The University of British Columbia, Okanagan Campus, Kelowna, Canada

^{2*} Department of Mathematics and Statistics, The University of British Columbia, Okanagan Campus, Kelowna, Canada

1. Abstract

The ensuing study will be a part of the author's master dissertation regarding the recoverable energy from the artificial wind generated from high-speed vehicular traffic on highways. Thanks to the development and progress of some numerical methods like the overset grid and dynamic fluid-body interaction (DFBI) solvers, replicating the physical situation on expressways inside a computational fluid dynamic (CFD) simulation is possible. However, the huge size of the domain in conjunction with the relatively fine grid required for a typical large eddy simulation (LES) modeling will be the characteristics of this numerical study. Among the existing solutions, splitting the computational domain through which only the inner half of the vehicles is adjacent to the rotor can be a promising solution. This report covers a series of numerical simulations conducted in StarCCM+ CFD package to compare the flow field behind Ahmed Body in two modes of full and half geometries. For each case eight probe planes are placed at different locations in the rear of vehicles recording some physical quantities at certain time steps. By using the capabilities of python libraries, an algorithm is designed to generate an average CSV file based on all of the produced CSV files throughout the runtime. Data processing is done by using the excel spreadsheet software and the results of this processing are manifested in some plots generated by Tableau software. In addition to the tableau plots, for each probe planes, surface contours were plotted using MATLAB to have a better understanding of the flow field.

2. Introduction

As mentioned before, the produced *localized wind energy* as the result of high-speed moving vehicles has a very appreciable potential considering the traffic flow, especially on expressways. In this regard, the implementation of VAWTs for energy recovery from this source is a very fresh and novel idea. Apart from some designs and concepts which still are in

progress, the amount of available data in the literature is very scarce and is only limited to some conducted numerical works with so many assumptions. For instance, a multi-stage Savonius rotor combined with a solar panel was proposed by Taskin et al. [1] which can be planted in the median strip of expressways. In another effort by Krishnaprasanth et al. [2], a maglev turbine was designed specifically for the power generation from expressways. These works did not include any insights regarding the performance of rotors either analytically, numerically or experimentally. The feasibility of power generation by a 4-involute spiral bladed rotor (Fig. 1) in the median strip of a highway was demonstrated [3]. Unfortunately, this study



Figure 1. Involute spiral design for a VAWT placed to recover energy in the median strip of a highway [3].

provides no information regarding the conditions of conducted tests including traffic regime, rotor properties, highway's specification and etc. with very simplified assumptions. It should be noted again that the idea of harvesting energy from the vehicular traffic has been proposed for around a decade with some patented designs [4-6]. Since there have not been any detailed investigations regarding the characteristics of this energy source highly likely explains why still the international market has still hesitated towards this source.

The abovementioned study considering all of its merits did not include any energy extracting device such as a VAWT. To the best knowledge of this author, still, there is no detailed study highlighting the performance of any extracting energy device from real traffic flow. Concerning this lack of data, one plausible reason might return to the difficulty of performing such experimental tests since there is no regular pattern in traffic flows. Moreover, there are lots of involved parameters and uncertainties which add more complexities to the process of designing experiment, data mining and decision making. Therefore, performing numerical

simulations can be a good alternative to obtain some first-hand impressions about the aerodynamic performance of a VAWT. More importantly, a better understanding of the mechanism of power generation, flow detail in any point of interest, and the correlation between the designed flow traffic and rotor can be obtained.

The first systematic numerical study investigating the performance of a VAWT in the wake of a vehicle was conducted by Tian et al. [7]. In their study, a Banki type rotor was placed on the medians of the highway and two factors of vehicle speed (15, 20, 25, 30 m/s) and the gap between the rotor and moving car (0.5, 1, 1.5, 2 m) was considered as the study parameters. They used shear stress transport (SST) $k_t\text{-}\omega$ turbulence model with second-order finite volume discretization scheme to solve the incompressible Reynolds-averaged Navier-Stokes (RANS) equations. Their numerical set-up illustrating the domain and boundary conditions is shown in Fig. 2. One of the great and inspiring aspects of this study was the utilization of morphing cell with the dynamic layering to realize the translational motion of the car. It was found given the best conditions; the rotor was able to extract 100.49 J energy from the wake of the car. Also, the wake of the car was similar to the Kármán vortex street comprised of many swirling vortices (Fig. 3) introduced as the main component of wake energy. However, there are some remarks worth mentioning here. First of all, the angular velocity of the rotor has been fixed which is a great simplification for this type of problems. Moreover, the traffic flow included only a single car and other case scenarios including more vehicles either in one or opposite directions have not been considered.

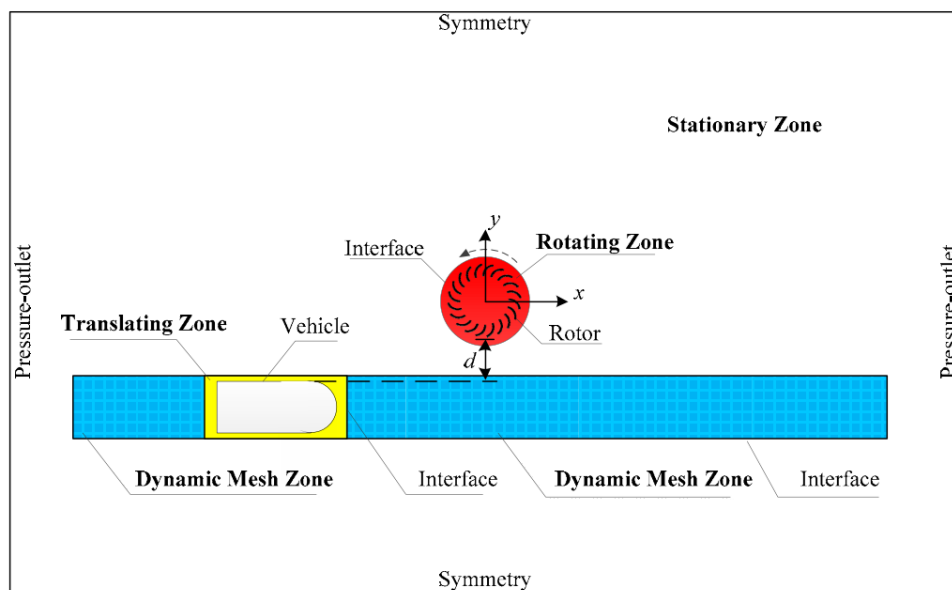


Figure 2. Computational domain and boundary conditions used in ref. [7].

The latest study by Tian et al. [8] is by far the most detailed and accurate modeling which benefits from a series of 3D numerical simulations. Moreover, the impact of traffic direction and different lanes have been considered by assuming five typical situations including one car on the passing lane, one bus on the passing lane, two cars approaching from two opposite passing lanes, one car on the fast-main lane and one bus on the fast-main lane (Fig. 4).

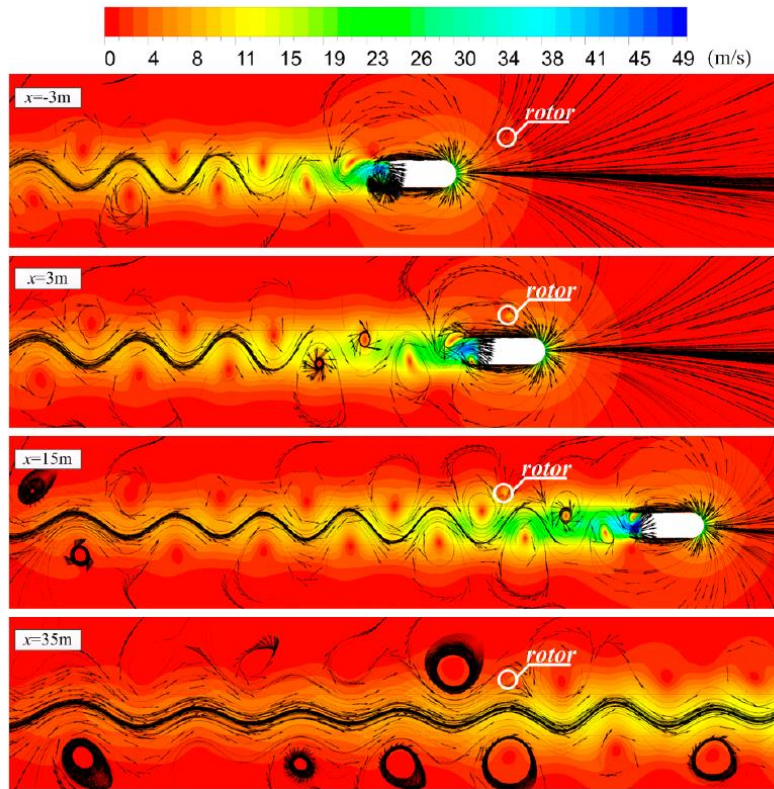


Figure 3. Velocity contour and streamlines in the flow field generated by vehicular traffic. Different contours are illustrated at different position of car with respect to the rotor [7].

The numerical method and boundary conditions illustrated in Fig. 5 is identical with their previous study [7] apart from pressure outlet which this time has been configured on the top and also side faces as well. Similarly, the rotor was modeled with a prescribed and fixed rotational speed. There are several important results found in their study worth discussing. The power generated by the bus moving in the passing lane exceeds other cases. This can be related to the bigger so-called “block and side region” which apparently is made up of high-velocity air transported by the vehicle, which is mainly concentrated in the frontal region of the vehicle as demonstrated in Fig. 6. More importantly, the passing lane traffic was not able to have any impact on the rotor in terms of power production leading to the importance of traffic flow in the passing lane.

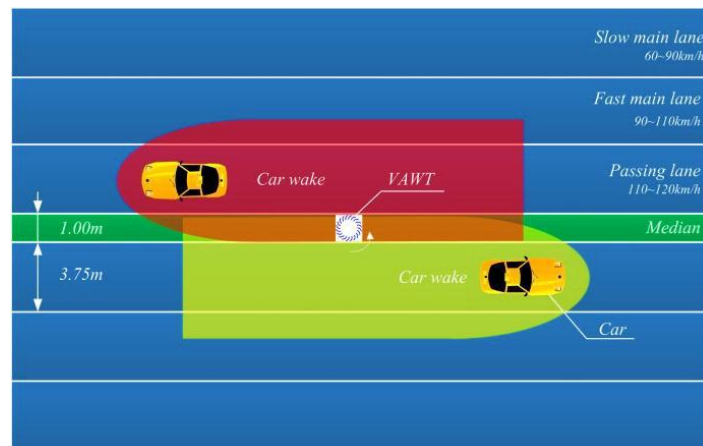


Figure 4. Definition of different lanes in the Chinese highway based on the dimensional and speed considerations used in the Ref. [8].

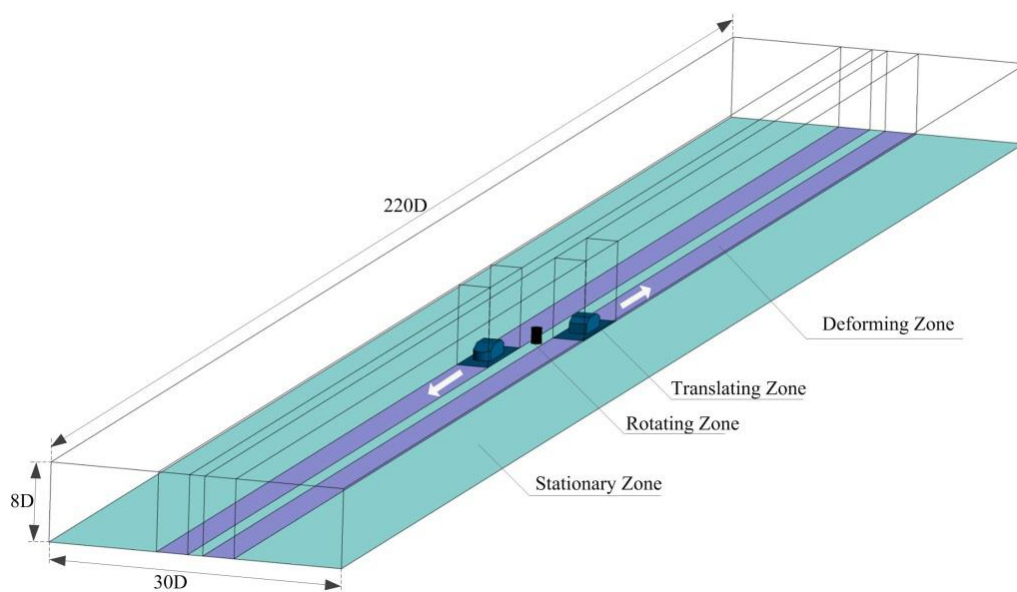


Figure 5. Computational domain and the boundary conditions [8].

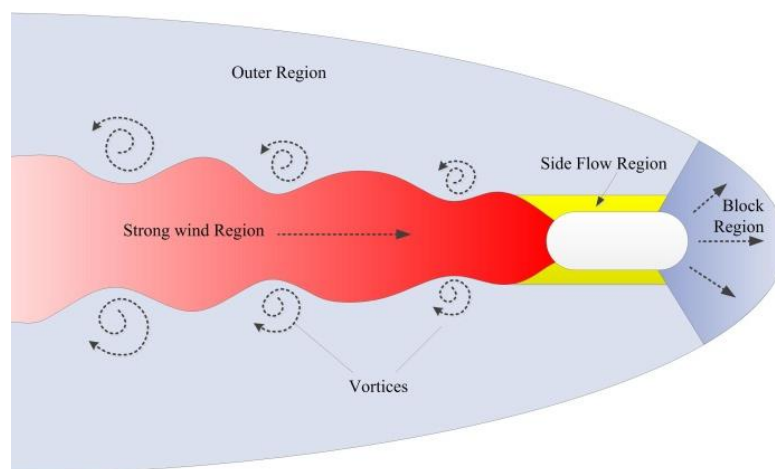


Figure 6. Schematic of the flow field around the bus [8].

3. Problem Description

Fig 7. shows a schematic of the computational domain which highlights the physical assumptions and numerical techniques to resolve the problem. The speed, number, and arrangement of vehicles will vary according to the traffic-shape implemented for each case. The size of the computational domain, specifically, its length (L) is an important parameter which affects the simulation in the following ways:

- 1- The number of vehicles on each lane owing to the existing regulations regarding spacing between vehicles. This distance is determined by the traffic legislations of each country or even state. Generally, the two seconds rule¹ and some correlations are widely accepted. In this work, the Eq. (1) will serve as the employed correlation where S and V are the spacing and vehicle speed, respectively [9].

$$S = 21 + 1.1V \quad (1)$$

- 2- The number of cells in the computational domain is directly proportional to the length of the domain.

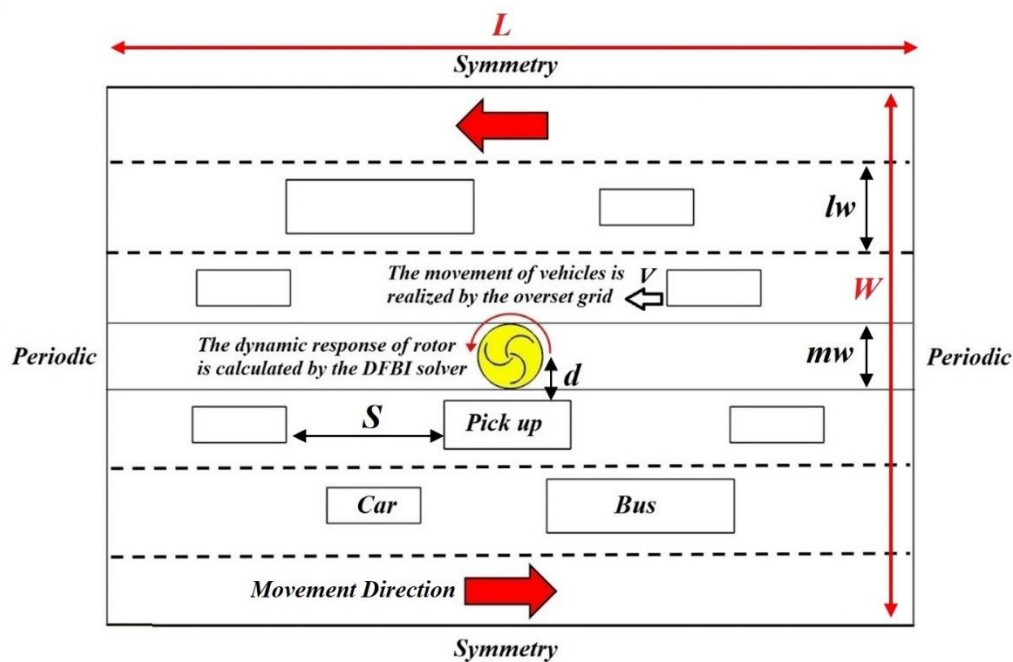


Figure 7. Schematic of simulation's structure in terms of physical and numerical configurations.

- 3- The larger domain allows the vehicle to travel a greater distance from the upfront to the downwind of the rotor. Hypothetically, the rotor will experience a more realistic localized

¹ Defined as the distance traveled in 2s at highway speeds.

wind profile in terms of flow structures from the approaching moving objects considering more time given to them to build their associated side and rear vortices. Similarly, and even more importantly, better certainty can be obtained regarding the effective distance in which the rotor is still under the influence of vehicle in the downwind.

After a parametric study, the computational domain shown in Fig. 8 was selected to serve in our main test cases. By taking a closer look it can be seen that this domain is very huge for a CFD simulation especially using LES turbulence model. The total number of cells in the presence of vehicles can even exceed 20 million leading to very large files and very time demanding runtimes. Our early analyses show that each simulation would take between 2-3 weeks and at each time step (0.001s) occupies around 12.1 GB on memory. Given the total

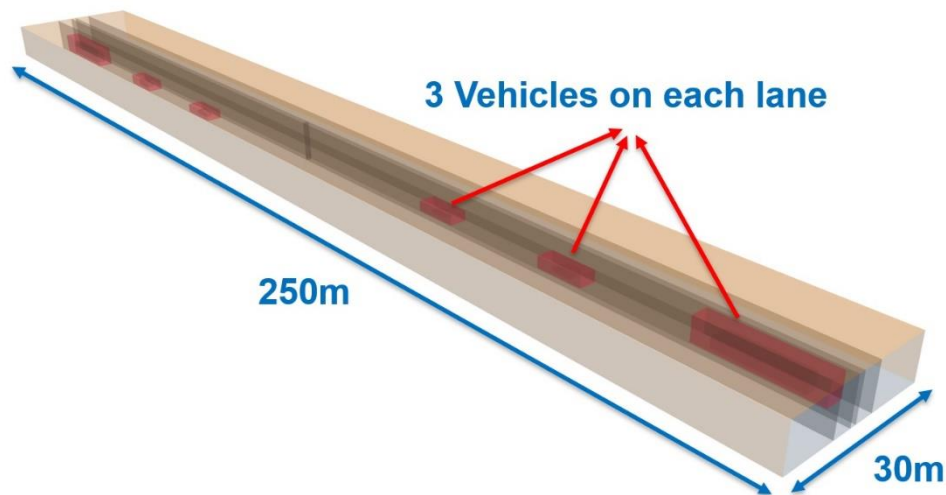


Figure 8. Schematic of computational domain and its dimensions.

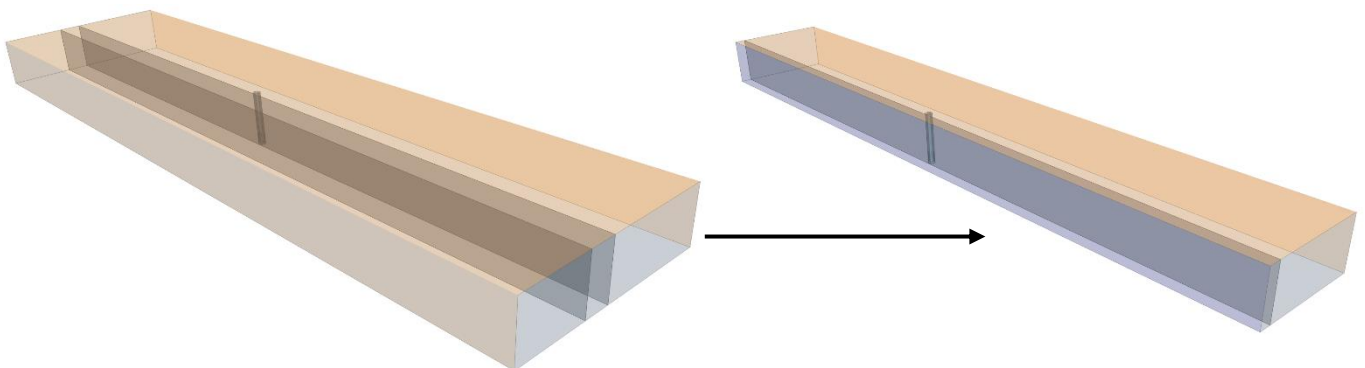


Figure 9. Splitting the computational domain to reduce the number of cells.

runtime, which is 6.8 sec, the required space for storing all states of simulation easily exceed 82.28 TB. This number even rises to 1.16 PB for all cases. These figures simply enforce us to

implement a strategy to handle the problem. The only plausible solution to cut the number of cells without affecting the simulation is to split the lanes into half and consider the inner ones which are adjacent to the rotor region as shown in Fig. 9. The validity of this solution has to be examined through a systematic approach which will be the target of this report.

4. Numerical Methodology

Generally, vehicles are the very complex bluff bodies and the associated flow field around them is very complex. Generating a grid around the vehicle using conventional methods would be very difficult and time-consuming. Hence, researchers usually consider some simplified reference geometries to represent a vehicle. One of these models is called “Ahmed Body” [10-12] which is used in our analysis (Fig. 10). To address our main problem explained in the introduction, three simulations (3D, Semi-3D, 2D) have been designed to see how the flow field in the downwind of the vehicle varies. These simulations have been carried out by solving the continuity and unsteady form of Navier-Stokes equations (Eqs. 2 and 3) using finite volume discretization in Star CCM+ solver. The total run time and the time step are 2 and 0.001 seconds, respectively.

$$\frac{\partial \bar{u}_i}{\partial x_i} = 0 \quad (2)$$

$$\frac{\partial \bar{u}_i}{\partial t} + \bar{u}_j \frac{\partial \bar{u}_i}{\partial x_j} = -\frac{1}{\rho} \frac{\partial \bar{P}}{\partial x_i} + \frac{\partial}{\partial x_j} \left(\nu \frac{\partial \bar{u}_i}{\partial x_j} \right) - \rho \left[2 \cdot \vec{\omega} \times \vec{W} + \vec{\omega} \times \vec{\omega} \times \vec{r} \right] + \frac{\partial \tau_{ij}}{\partial x_j} \quad (3)$$

where \bar{u}_i and \bar{P} are averaged velocity and pressure, respectively. Also, W , ω , ρ and ν are relative velocity, rotational speed, density, and kinematic viscosity, respectively. Furthermore, $\bar{\tau}$ is the specific Reynolds stress tensor described as:

$$\tau_{ij} = \overline{u'_i u'_j} \quad (4)$$



Figure 10. Ahmed body full (left) and half (right) geometries.

4.1. Data Gathering

By defining a series of probe lines (for 2D) and probe planes (for Semi-3D and 3D cases) placed at different locations from the rear of the vehicle (Fig. 11), a collection of CSV files were acquired. The solver was configured to generate each file with a time step of 0.01 sec and

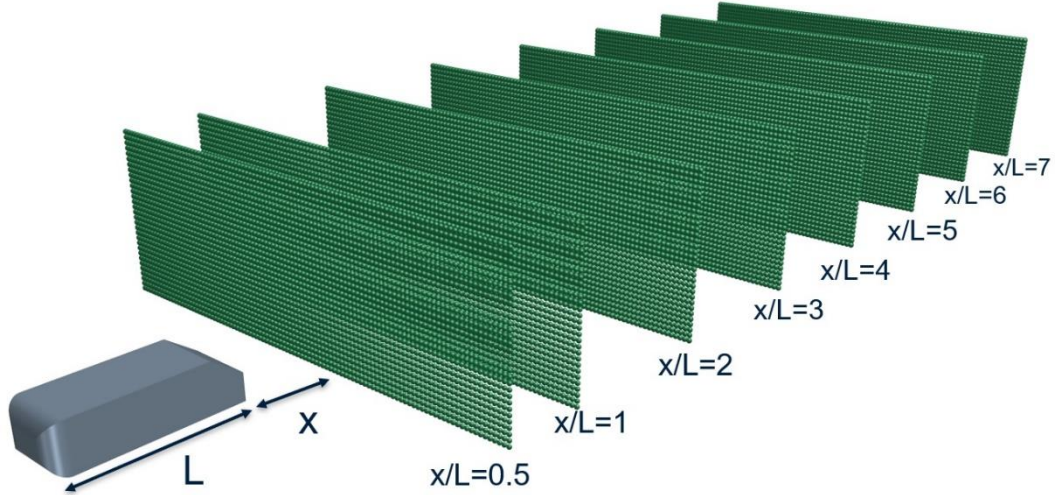


Figure 11. Different probe planes at the rear of the vehicle store the necessary information.

the recording was performed for the latter half of the simulation, namely, 1-2 sec. The reason for that is to avoid some initialization errors in the calculation of the flow field. Each file encompasses the probe points coordinate and the value of vorticity and velocity as the chosen vector fields as shown in Fig. 12. For each simulation and in total 100 files were generated.

	A	B	C	D	E	F	G	H	I	J	K	L	M	N	O	P	Q	R
1	Vorticity: Magnitude (1/s)	Vorticity[i] (1/s)	Vorticity[j] (1/s)	Vorticity[k] (1/s)	Velocity: Magnitude (m/s)	Velocity[i] (m/s)	Velocity[j] (m/s)	Velocity[k] (m/s)	X (m)	Y (m)	Z (m)							
2	0.79529703	-3.21E-16	-0.79529703	-1.61E-16	41.84306342	-0.292807294	4.74E-17	-41.84203891	1.5	0.0500000001	-2.088							
3	0.79529703	-3.21E-16	-0.79529703	-1.61E-16	41.84306342	-0.292807294	4.74E-17	-41.84203891	1.47	0.0500000001	-2.088							
4	0.935220559	-4.16E-16	-0.935220559	5.87E-16	41.84701759	-0.420696346	-2.03E-17	-41.84490286	1.44	0.0500000001	-2.088							
5	0.935220559	-4.16E-16	-0.935220559	5.87E-16	41.84701759	-0.420696346	-2.03E-17	-41.84490286	1.41	0.0500000001	-2.088							
6	0.935220559	-4.16E-16	-0.935220559	5.87E-16	41.84701759	-0.420696346	-2.03E-17	-41.84490286	1.38	0.0500000001	-2.088							
7	0.935220559	-4.16E-16	-0.935220559	5.87E-16	41.84701759	-0.420696346	-2.03E-17	-41.84490286	1.35	0.0500000001	-2.088							
8	0.958214482	1.82E-16	-0.958214482	-1.65E-17	41.84405943	-0.449761663	-7.56E-17	-41.84164222	1.32	0.0500000001	-2.088							
9	0.958214482	1.82E-16	-0.958214482	-1.65E-17	41.84405943	-0.449761663	-7.56E-17	-41.84164222	1.29	0.0500000001	-2.088							
10	0.958214482	1.82E-16	-0.958214482	-1.65E-17	41.84405943	-0.449761663	-7.56E-17	-41.84164222	1.26	0.0500000001	-2.088							
11	1.143193848	-1.39E-16	-1.143193848	3.40E-16	41.76257797	-0.587344218	-1.97E-17	-41.7584476	1.23	0.0500000001	-2.088							
12	1.143193848	-1.39E-16	-1.143193848	3.40E-16	41.76257797	-0.587344218	-1.97E-17	-41.7584476	1.2	0.0500000001	-2.088							
13	1.143193848	-1.39E-16	-1.143193848	3.40E-16	41.76257797	-0.587344218	-1.97E-17	-41.7584476	1.17	0.0500000001	-2.088							
14	1.253156993	1.15E-15	-1.253156993	-4.98E-16	41.65627425	-0.619541828	-1.30E-16	-41.65166686	1.14	0.0500000001	-2.088							
15	1.253156993	1.15E-15	-1.253156993	-4.98E-16	41.65627425	-0.619541828	-1.30E-16	-41.65166686	1.11	0.0500000001	-2.088							
16	1.253156993	1.15E-15	-1.253156993	-4.98E-16	41.65627425	-0.619541828	-1.30E-16	-41.65166686	1.08	0.0500000001	-2.088							
17	1.26986717	2.32E-15	-1.26986717	9.58E-16	41.44017104	-0.767812333	5.92E-17	-41.43305734	1.05	0.0500000001	-2.088							
18	1.26986717	2.32E-15	-1.26986717	9.58E-16	41.44017104	-0.767812333	5.92E-17	-41.43305734	1.02	0.0500000001	-2.088							
19	1.26986717	2.32E-15	-1.26986717	9.58E-16	41.44017104	-0.767812333	5.92E-17	-41.43305734	0.99	0.0500000001	-2.088							
20	1.429982608	-9.67E-16	-1.429982608	7.76E-16	41.17956772	-0.829328384	-2.36E-16	-41.17121582	0.96	0.0500000001	-2.088							
21	1.429982608	-9.67E-16	-1.429982608	7.76E-16	41.17956772	-0.829328384	-2.36E-16	-41.17121582	0.93	0.0500000001	-2.088							
22	1.245799258	7.94E-17	-1.245799258	-1.49E-15	40.78503132	-1.008552861	-6.63E-17	-40.77255941	0.9	0.0500000001	-2.088							
23	1.245799258	7.94E-17	-1.245799258	-1.49E-15	40.78503132	-1.008552861	-6.63E-17	-40.77255941	0.87	0.0500000001	-2.088							
24	1.480709843	8.07E-16	-1.480709843	3.35E-16	40.33225031	-1.128541525	-5.10E-17	-40.31645829	0.84	0.0500000001	-2.088							
25	1.480709843	8.07E-16	-1.480709843	3.35E-16	40.33225031	-1.128541525	-5.10E-17	-40.31645829	0.81	0.0500000001	-2.088							
26	1.183351169	-3.67E-17	-1.183351169	1.30E-16	39.74181333	-1.351563533	-1.16E-16	-39.71882429	0.78	0.0500000001	-2.088							
27	1.183351169	-3.67E-17	-1.183351169	1.30E-16	39.74181333	-1.351563533	-1.16E-16	-39.71882429	0.75	0.0500000001	-2.088							
28	1.424853144	1.97E-15	-1.424853144	-5.88E-15	39.08208883	-1.54633778	-7.33E-17	-39.05148533	0.72	0.0500000001	-2.088							
29	1.424853144	1.97E-15	-1.424853144	-5.88E-15	39.08208883	-1.54633778	-7.33E-17	-39.05148533	0.69	0.0500000001	-2.088							

Figure 12. The generated CSV file by the solver at each time step.

However, it is worth pointing out that the CSV file for the 2D case contains all the probe lines where for the 3D cases the information for each probe plane is stored in different files.

4.2. Data Munging

One of the key aspects of this study is to analyze the generated CSV files. But due to the huge number of files, processing these files individually is impossible and making a connection between them is also a very challenging task. Hence, there is a great necessity to perform the data analysis on a representative file for each probe location. Ideally, each cell of this file would be the average of corresponding cells at each individual file. By taking advantage of python and especially the additional libraries like numpy and pandas, we were able to write a program fulfilling the required task. Fig. 13 represents the python code which finds the files in a given

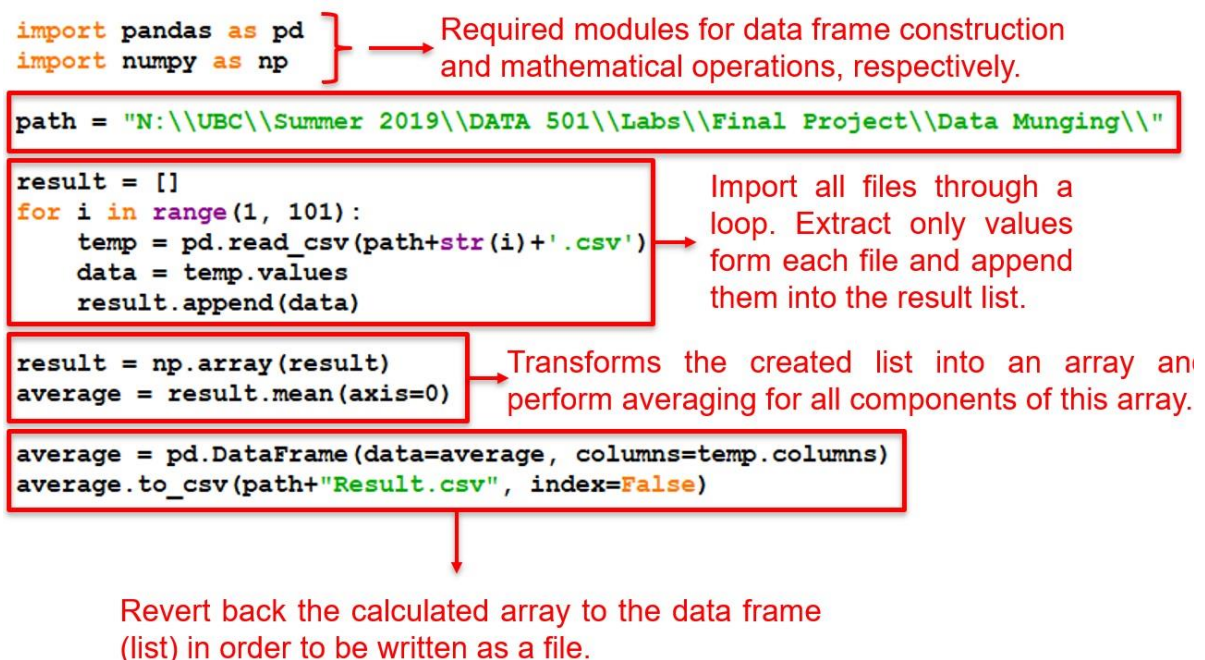


Figure 13. The written algorithm in the python code to obtain an average file.

path and then import them into a list. Each item of this list is an individual file. However, due to the inherent nature of a list in python, these items cannot be used in calculations directly. By using the numpy capability this list then will be converted to an array. Numpy has some inbuilt functions which can be used directly such as mean to perform averaging for a collection of components. The resulting array; however, is not in a suitable format for exporting. Therefore, it is required that this array would be reverted back to a list by using the Dataframe function which exists in the pandas module.

4.3. Data Processing

Having generated the average file for each case, these files will be analyzed in excel to extract useful information. For the 2D case, information has been spread in different worksheets corresponding to the location of probe lines in the z-direction. Using the inbuilt functions in excel including AVERAGE and STDEV.P the average and standard deviations for streamwise velocity (velocity[k]), velocity magnitude, and vorticity magnitude are calculated, respectively. In addition, the coefficient of variations CV is another calculated quantity used in the data analysis process. The CV is a statistical term commonly serving as a standardized measure for the dispersion calculation for a set of data. In other words, this parameter can be used to indicate the variation of a quantity with respect to the mean value of that quantity for a population defined as follows

$$\sigma = \frac{\sqrt{\sum_{i=1}^n (X_i - \bar{X})^2}}{\bar{X}} \quad (4)$$

$$CV = \frac{\sigma}{\bar{X}} \quad (5)$$

σ and \bar{X} are the standard deviation and the average values for a set of data obtained through the foregoing probe points, respectively. All of these values have been summarized in an excel file called Comparison (Fig. 14) to quantitatively be used in a systematic comparison to see how much the dimension and geometry truncation will impact on the flow field behind the vehicle.

V1															
	A	B	C	D	E	F	G	H	I	J	K	L	M	N	O
1			Streamwise Velocity				Velocity Magnitude				Vorticity Magnitude				
2		x/L	2D	Semi-3D	3D		2D	Semi-3D	3D		2D	Semi-3D	3D		
3	Averaged Values	0.5	39.5514	40.0232	40.0453		42.715	40.1205	40.1271		41.0647	19.0898	17.2748		
4		1	39.6932	40.0732	40.077		42.3446	40.1161	40.111		33.4172	14.3056	12.2745		
5		2	39.7945	40.101	40.1124		42.2631	40.1248	40.132		33.7151	11.8738	10.4108		
6		3	39.7452	40.1026	40.1157		42.1124	40.1204	40.1308		34.7749	11.4272	9.73393		
7		4	39.5868	40.1084	40.123		41.7996	40.1222	40.1349		37.4108	10.8983	9.31338		
8		5	39.2626	40.1175	40.1303		41.2231	40.1288	40.1395		38.8974	10.5243	9.06851		
9		6	38.8045	40.1202	40.1375		40.362	40.1297	40.145		38.4323	10.2859	8.89066		
10	7	38.1693	40.1299	40.1565		39.2735	40.1375	40.1624		33.8283	8.73231	8.30378			
11															
12		x/L	2D	Semi-3D	3D		2D	Semi-3D	3D		2D	Semi-3D	3D		
13	Standard Deviation	0.5	6.42016	2.19178	2.27158		0.58738	1.7579	1.90988		89.1342	97.6999	98.7606		
14		1	5.90982	1.38372	1.37812		1.78945	1.20187	1.23416		56.7591	61.2281	56.6005		
15		2	5.80327	1.06193	1.03949		2.44788	0.98008	0.96325		47.3095	38.0014	37.0874		
16		3	5.09552	0.9808	0.96649		2.14869	0.92865	0.91577		43.4997	30.5501	29.3541		
17		4	5.21532	0.9258	0.90294		2.61437	0.89069	0.86738		41.2949	26.1563	24.8414		
18		5	7.13104	0.88717	0.87517		4.94915	0.86069	0.85037		36.9917	23.7799	22.3771		
19		6	9.34517	0.88912	0.86612		7.63662	0.86858	0.84725		32.8732	23.0831	21.1937		
20	7	10.309	0.90472	0.87891		9.43575	0.88815	0.86523		25.4394	19.0207	20.0417			
21															
22		x/L	2D	Semi-3D	3D		2D	Semi-3D	3D		2D	Semi-3D	3D		
23	Variation Coefficient	0.5	0.16232	0.05476	0.05673		0.01375	0.04382	0.0476		2.17058	5.1179	5.71703		
24		1	0.14889	0.03453	0.03439		0.04226	0.02996	0.03077		1.6985	4.28001	4.61124		
25		2	0.14583	0.02648	0.02591		0.05792	0.02443	0.024		1.40321	3.20044	3.56239		
26		3	0.1282	0.02446	0.02409		0.05102	0.02315	0.02282		1.25089	2.67346	3.01564		
27		4	0.13174	0.02308	0.0225		0.06255	0.0222	0.02161		1.10382	2.40002	2.66729		
28		5	0.18162	0.02211	0.02181		0.12006	0.02145	0.02119		0.95101	2.25952	2.46756		
29		6	0.24083	0.02216	0.02158		0.1892	0.02164	0.0211		0.85535	2.24414	2.38382		
30	7	0.27009	0.02254	0.02189		0.24026	0.02213	0.02154		0.75201	2.1782	2.41356			
	►	Data	Avg S Vel	Avg Vel M	Avg Vor M	STDev S Vel	STDev Vel M	STDev Vor M		Cv S Vel	Cv Vel M	Cv ... (4)	⋮	◀	

Figure 14. The processed data in excel which will be used for further data visualizations.

5. Result and Discussion

5.1. Tableau plots

Figs. 15 and 16 illustrate the averaged values for velocity and vorticity magnitudes for different locations, respectively plotted by tableau 19.2 software. Both 3D cases illustrate similar behaviors while the 2D case does not follow the trend of 3D cases on the ground of trend and values. This discrepancy becomes significant in predicting the vorticity magnitudes. There are several reasons for these behaviors worth discussing. Firstly, although the frequency of instantaneous shed vortices might be different for semi-3D and 3D cases, the overall shed vortices over a period of time are similar. Secondly, due to the weaker dissipation rate in 2D dimension, the disturbances and irregularities of flow are likely to be much stronger in far distances compared to 3D cases.

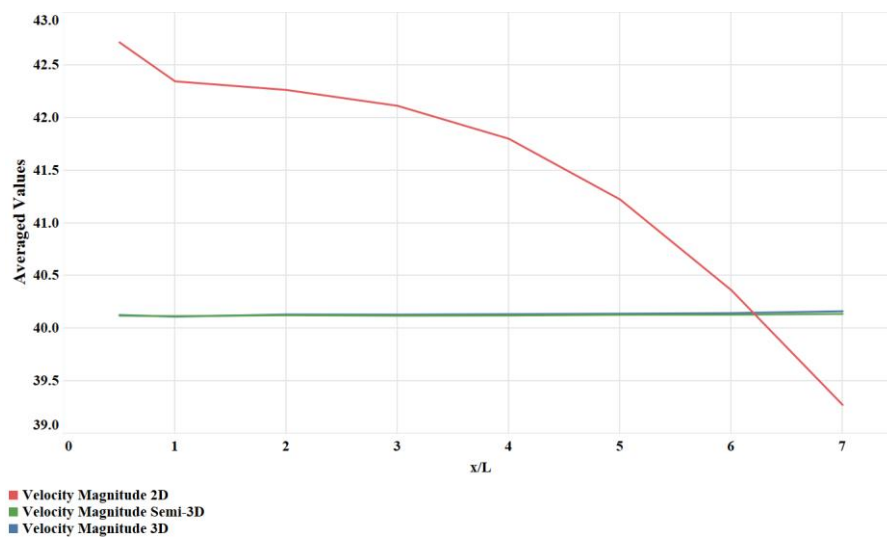


Figure 15. Velocity magnitude at different probe planes.

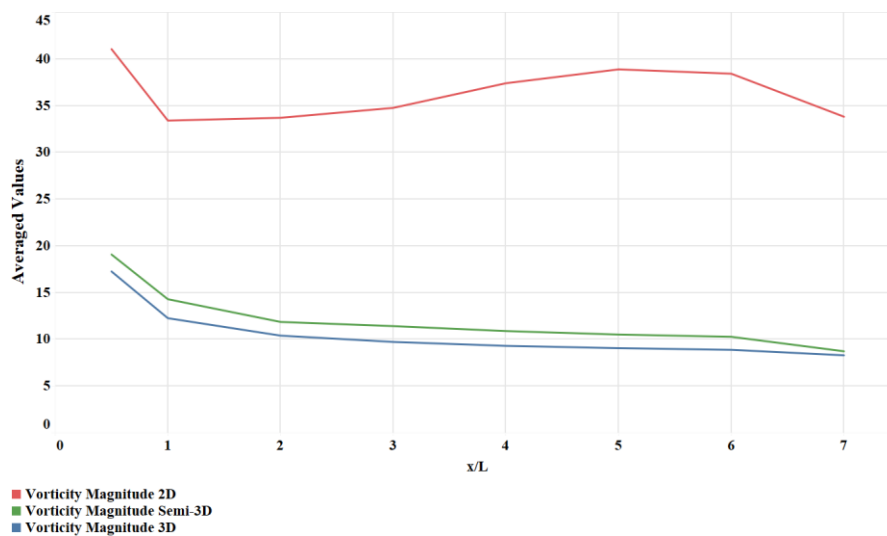


Figure 16. Vorticity magnitude at different probe planes.

Standard deviations for both quantities are represented in Figs. 17 and 18. Similarly, no deviations were found between the two 3D cases and they have very good agreements. Fig 17 reveals a strong contrast in the predicted velocity field, especially, in far distances between 2D and 3D cases. As σ tends to decrease in the 3D cases because of proper turbulence dissipation yielding to a uniform and low value across all locations, this figure increases with a steep slope for the 2D case. This problem seems to be less apparent for the vorticity magnitude as is apparent in Fig. 18.

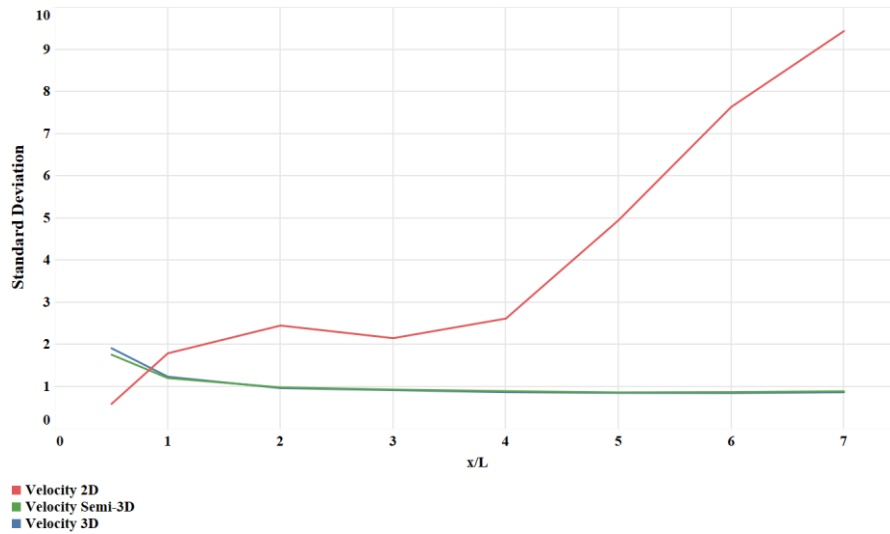


Figure 17. The standard deviation for velocity magnitude at different probe planes.

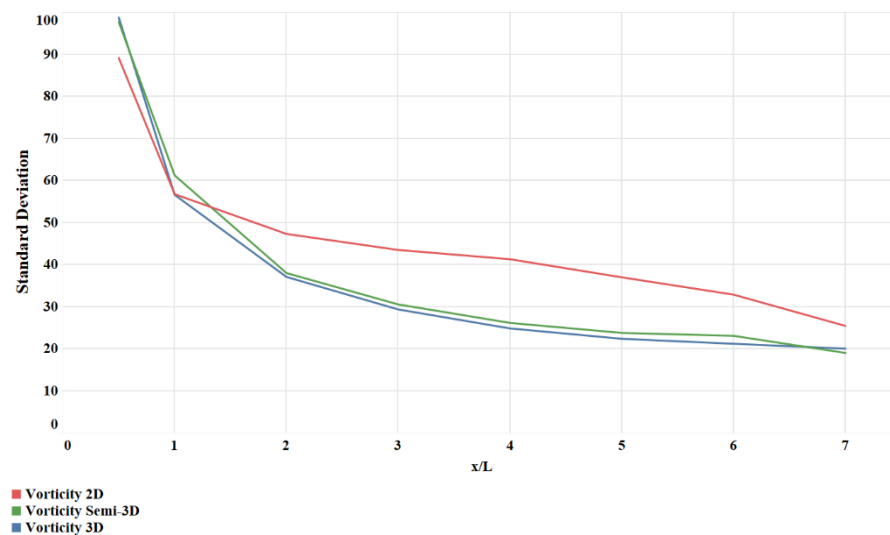


Figure 18. The standard deviation for vorticity magnitude at different probe planes.

5.2. MATLAB surface contours

In addition to previous plots drawn by tableau, a series of surface contours were plotted using MATLAB to visually understand and compare vorticity magnitude variations across different

locations. These contours are presented for four different probe planes (Fig. 19). These plots show that not only the two 3D cases are similar in terms of averaged values, but they share almost an exact flow field structure. It is interesting to see as the distance increases the region where the disturbances are concentrated becomes wider but less intensified. This is due to the fact that the vortex shedding is three-dimensional propagation phenomena but mostly in the stream and spanwise directions.

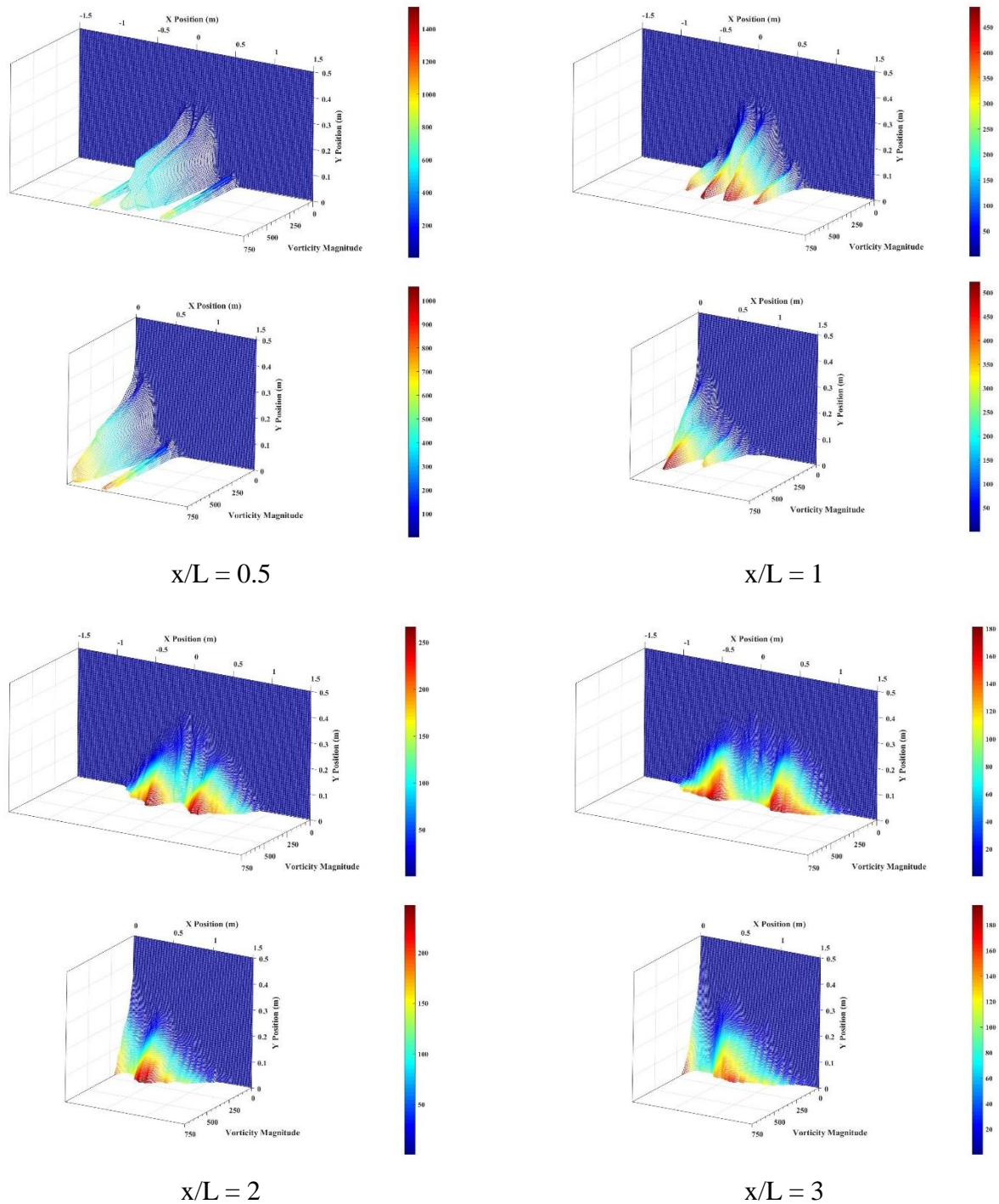


Figure 19. Surface contours plotted for four different probe planes.

6. Conclusion

This paper investigated a novel approach to address a common issue in the simulation of vast domains where time and computational resources are limited. Different techniques and software were implemented in tandem to perform data munging, analysis, and visualization. Based on the attained result:

- 1- The observed flow field for the full and semi-3D cases was almost identical quantitatively and qualitatively.
- 2- The discrepancy between 2D and 3D cases was significant, and the relative error for the 2D case even reached to 100%.
- 3- The trendlines found in the tableau plots all agreed well with the established theory regarding the bluff body aerodynamics.

7. References

1. Taskin, S.; Dursun, B. Performance assessment of a combined solar and wind system. Arab. J. Forence Eng. 2009, 34, 217–227.
2. Krishnaprasanth, B.; Akshaya, P.R.; Manivannan, L.; Dhivya, N.A. new fangled highway wind power generation. IJRASET 2016, 4, 31–34.
3. Murodiya, R.; Naidu, H. Design and Fabrication of Vertical Wind Turbine for Power Generation at Highway Medians. Int. Eng. J. Res. Dev. 2016, 1, 1–10.
4. Sakamaki M. Tunnel Installation type aerogenerator. Japan Patent JP56034979A; Filed April 07, 1981.
5. Wiegel TF, Stevens KC. Traffic-driven wind generator. United States Patent US007098553B2; Filed January 12, 2005.
6. Fein GS, Merritt E. Genedics Clean Energy, Llc., System and method for creating a networked infrastructure distribution platform of small fixed and vehicle-based wind energy gathering devices along roadways. United States Patent US 7741727 B2; Filed December 22, 2006.
7. Wenlong Tian, Zhaoyong Mao, Yukai Li, Numerical Simulations of a VAWT in the Wake of a Moving Car, Energies 2017, 10, 478; doi:10.3390/en10040478.

8. Wenlong Tian, Zhaoyong Mao, Xinyu An, Baoshou Zhang, Haibing Wen, Numerical study of energy recovery from the wakes of moving vehicles on highways by using vertical axis wind turbine, *Energy* (2017), doi: 10.1016/j.energy.2017.07.172.
9. Cornell Local Roads Program, 1975, "Highway Design for Motor Vehicles: A Historical Review," *Public Roads*, 39(3), pp. 1–22.
10. Ahmed, S.R., Ramm, G., Faltin, G.: Some Salient Features of the Time -Averaged Ground Vehicle Wake. SAE-Paper, 840300 (1984).
11. Bruneau, C.-H., Mortazavi, I., Gilliéron, P.: Passive control around the two-dimensional square back Ahmed body using porous devices. *J. Fluids Eng.* 130, 1–33 (2008).
12. C.H. Bruneau, E. Creusé, D. Depeyras, P. Gilliéron, and I. Mortazavi, Numerical Simulation and Control of the 3D Flow Around Ahmed Body, *Proceedings of the Sixth International Conference on Computational Fluid Dynamics, ICCFD6*, St Petersburg, Russia, on July 12-16, 2010, DOI 10.1007/978-3-642-17884-9_36.